Journal of Radiation Research, 2014, 55, 191–199
doi: 10.1093/jrr/rrt100 Advance Access Publication 26 August 2013

Evaluation of imaging performance of megavoltage cone-beam CT over an extended period

Iori SUMIDA[1,2,*], Hajime YAMAGUCHI[2], Hisao KIZAKI[2], Yuji YAMADA[2], Masahiko KOIZUMI[3], Yasuo YOSHIOKA[3], Kazuhiko OGAWA[3], Naoya KAKIMOTO[1], Shumei MURAKAMI[1] and Souhei FURUKAWA[1]

[1]Department of Oral and Maxillofacial Radiology, Osaka University Graduate School of Dentistry, 1-8 Yamada-oka, Suita, Osaka, 565-0871, Japan
[2]Department of Radiation Oncology, NTT West Osaka Hospital, 2-6-40 Karasugatsuji, Tennoji-ku, Osaka, 543-8922, Japan
[3]Department of Radiation Oncology, Osaka University Graduate School of Medicine, 2-2 Yamada-oka, Suita, Osaka, 565-0871, Japan
*Corresponding author. Department of Oral and Maxillofacial Radiology, Osaka University Graduate School of Dentistry, 1–8 Yamada-oka, Suita, Osaka, 565-0871 Japan. Tel: +81-6-6879-2967; Fax: +81-6-6879-2970; Email: isumida@dent.osaka-u.ac.jp

(Received 26 November 2012; revised 1 July 2013; accepted 18 July 2013)

A linear accelerator vendor and the AAPM TG-142 report propose that quality assurance testing for image-guided devices such megavoltage cone-beam CT (MV-CBCT) be conducted on a monthly basis. In clinical settings, however, unpredictable errors such as image artifacts can occur even when quality assurance results performed at this frequency are within tolerance limits. Here, we evaluated the imaging performance of MV-CBCT on a weekly basis for ~ 1 year using a Siemens ONCOR machine with a 6-MV X-ray and an image-quality phantom. Image acquisition was undertaken using 15 monitor units. Geometric distortion was evaluated with beads evenly distributed in the phantom, and the results were compared with the expected position in three dimensions. Image-quality characteristics of the system were measured and assessed qualitatively and quantitatively, including image noise and uniformity, low-contrast resolution, high-contrast resolution and spatial resolution. All evaluations were performed 100 times each. For geometric distortion, deviation between the measured and expected values was within the tolerance limit of 2 mm. However, a subtle systematic error was found which meant that the phantom was rotated slightly in a clockwise manner, possibly due to geometry calibration of the MV-CBCT system. Regarding image noise and uniformity, two incidents over tolerance occurred in 100 measurements. This phenomenon disappeared after dose calibration of beam output for MV-CBCT. In contrast, all results for low-contrast resolution, high-contrast resolution and spatial resolution were within their respective tolerances.

Keywords: Cone-beam CT; QA; image-guided radiation therapy; IGRT; tolerance; calibration

INTRODUCTION

Image-guided radiation therapy (IGRT) during patient set-up prior to treatment delivery allows the patient to be positioned as closely as possible to the expected irradiation position. Several recent IGRT techniques include fan-beam CT [1–3], CT-on-rails [4], cone-beam CT (CBCT) [5–6], electronic portal imaging device (EPID) [7], ultrasound system [8] and infrared marker [9]. The first four of these techniques use X-rays in kilovoltage or megavoltage beam quality. Depending on beam quality, however, these techniques may include features such as image contrast between bony structures and soft tissues, and the presence metallic artifacts. Correct placement of the patient requires assurance of the performance of imaging devices in terms of both image quality and the lack of geometrical distortion related to the treatment room coordinates. These items should be confirmed stable within the institution's tolerance limits.

© The Author 2013. Published by Oxford University Press on behalf of The Japan Radiation Research Society and Japanese Society for Therapeutic Radiology and Oncology.
This is an Open Access article distributed under the terms of the Creative Commons Attribution Non-Commercial License (http://creativecommons.org/licenses/by-nc/3.0/), which permits unrestricted non-commercial use, distribution, and reproduction in any medium, provided the original work is properly cited.

Our department uses a megavoltage CBCT (MV-CBCT) for IGRT. MV-CBCT uses the same X-ray source and gantry as those used for treatment. It also uses the same EPID as for 2D imaging and thus eliminates the requirement for isocenter matching calibration. The linear accelerator (linac) vendor has proposed quality assurance (QA) instructions for MV-CBCT that should be performed on a monthly basis (referred to in Siemens MVision Physicist Self-Led Training). QA frequency has also been proposed in the American Association of Physicists in Medicine Task Group 142 report [10]. This instruction includes a check of image quality and geometric distortion in the three dimensions of lateral, longitudinal and vertical. The vendor also provides users with an original QA phantom for performing these tests. Based on the vendor instructions, the measurement protocol is defined with 15 monitor units (MU) with low-energy photons for irradiation and the use of a filter named 'smoothing head and neck'. A smoothing filter is applied to the reconstructed images to correct for the cupping effect due to the large amount of scatter inherent in the large field sizes in cone-beam geometry [11]. This filter has two naming options, 'pelvis' or 'head and neck', which corrects the cupping effect based on the size of the respective anatomical site, and 3 (head and neck region) or 5 MU (abdominal region) are used for image guidance in clinical settings to minimize the absorbed dose the patient receives during visualization [12, 13]. Even when the results of monthly QA performed with 15 MU are within tolerance, occasional errors such as streak artifacts, tyre-track artifacts, image non-uniformity, and undesirable contrast resolution have been noted in clinical use. The high-quality protocol suggested by the vendor for MV-CBCT at the linac for image quality assessment does not reflect the clinically recommended scan protocol, and subtle changes in imaging performance may occur within the 1-month testing period. In addition, if image quality does in fact decrease with time, a reduction in positioning or registration accuracy can be expected.

Here, to verify and track possible changes in QA results over periods of as long as one year, we performed the vendor-proposed QA on a weekly rather than monthly basis.

MATERIALS AND METHODS

Irradiation

An X-ray beam from an ONCOR Impression Plus dual photon energy linear accelerator (6 MV and 10 MV; Siemens Medical Systems, Erlangen, Germany) was used. Portal images were acquired with a Siemens OPTIVUE 1000 EPID (Siemens Medical Systems). The portal imager has matrices of 1024 × 1024 pixels with a physical size of 0.40 mm, giving an active area of 41 × 41 cm^2. A 3-mm copper plate overlays the sensitive layer of the EPID to remove low-energy photons; immediately beneath the copper plate is a scintillating layer of phosphor to transform incoming X-rays to visible photons, and then a pixel array implanted on the amorphous-Si panel to capture visible photons and convert them to electric charges. The charge signals are then read out and digitized by a 16-bit analog-to-digital converter. Source to image distance (SID) is changeable between 110 cm and 160 cm. QA measurements for MV-CBCT were rotational irradiation, which started at a gantry angle of 270° to 110° at a fixed SID of 145 cm with a 27.4 cm × 27.4 cm field size and low energy photons of 6 MV. SID was defined by the vendor.

Following insertion of the orthogonal tungsten wires (which are named the XRETIC plate and are matched to the mechanical isocenter) into the shadow tray, the Siemens image quality phantom (called the EMMA phantom, Siemens Medical Systems) was manually set to the isocenter using the wire shadow at gantry angles of 0°, 90° and 270° by matching the projection of the two orthogonal metal wires of the XRETIC plate with the reference lines of the phantom in the anterior and two lateral directions. After MV-CBCT irradiation, the system automatically reconstructs the CBCT image in a slice thickness of 1 mm and 256 × 256 matrices with filtered correction of cupping artifacts named 'smoothing head and neck', as described above. Voxel size was 1.07 mm × 1.07 mm × 1.00 mm in the lateral, vertical and longitudinal directions, respectively. Reconstructed image sets of a total of 274 slices were outputted and imported into our in-house software developed using CodeGear Delphi 2007. MV-CBCT imaging by the phantom analysis described below was performed 100 times per week for ~ 1 year. Evaluation of image quality with regard to low-contrast resolution, high-contrast resolution, and contrast-to-noise ratio was done by displaying transverse slices using a 5-mm multiple plane reconstruction view on the in-house software to reduce noise. This method is also based on the vendor's protocol.

Phantom analysis

The specification for the EMMA phantom is shown in Fig. 1. The EMMA phantom has three sets, each of four beads, that are used to check geometric distortion in three dimensions. The beads are distributed evenly around the circumference of

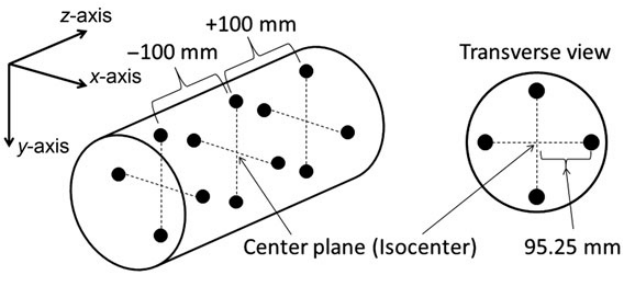

Fig. 1. The EMMA phantom geometry and bead configuration in 3D and transverse views. Four beads are evenly separated from the center of the phantom by 95.25 mm in transverse view. Transverse planes are located at intervals of 100 mm along the *z*-axis.

the phantom with z coordinates of 100 mm, 0 mm and – 100 mm for the superior, center and inferior slices, respectively. The four beads in each slice are located at the 3, 6, 9 and 12 o'clock positions, respectively. Each of the four beads is separated from the center of the phantom by +95.25 mm.

For the geometric distortion check, a reference point was manually placed at the center of each bead in the MV-CBCT image of the phantom using the in-house software, and then the position was compared with that of the nominal position. The deviation from the nominal position was measured for each bead. The tolerance level of 2 mm was defined by the vendor. Minimum pixel resolution for analysis in the in-house software was 0.27 mm in the lateral and vertical axes, and 0.23 mm in the longitudinal axis.

With regard to checking image quality, the EMMA phantom has a solid region that consists of four sections, namely: (a) a solid water section, (b) a low-contrast resolution section, (c) a spatial resolution section, and (d) a high-contrast resolution section. The solid region of the EMMA phantom is shown in Fig. 2.

Section (a) is a 40-mm uniform solid water cylinder that is used to check image noise and the uniformity of pixel values. On the central slice of this section, five circular regions of interest (ROIs) were automatically drawn on the image; one in the center and four in the periphery at the 3, 6, 9 and 12 o'clock positions at an equidistance of 69.6 mm from the center of the phantom, as shown in Fig. 3. The distance of 69.6 mm was determined to be suitably close to the edge of the phantom and was used for all analyses. The diameter of the ROI was 2 cm.

The mean pixel value and standard deviation for each ROI were calculated, and the pixel value was then compared with the vendor specification. Expected results for 6-MV acquisitions were as follows: the center ROI, which is numbered 2, should have (i) a standard deviation between +26 and +42, and (ii) a mean value of pixels between – 30 and +42. The difference between the mean pixel value of each peripheral ROI and the mean pixel value of the central ROI was calculated, and it was verified that the difference fell within the expected range of – 80 to +80. Image reconstruction artifacts due to dead pixels or wrong gantry rotation speed were also visually checked on each slice of this section.

Sections (b) and (d), which contain inserts of different material rods with various diameters inside a solid water background, are shown in Fig. 4.

The physical density and relative electron density of each material with respect to the background are presented in Table 1.

Low-contrast resolution was qualitatively checked by adjusting the window level and window width to preset values, and by counting the number of inserts of each material that were visible on the image. After the set of ROI included all inserts in each slice, the mean, maximum and minimum pixel values were calculated. The mean pixel value was used for the window level, and the difference between the minimum and maximum values was used for the window width in order to define the preset values for visual evaluation. Table 2 lists the circles that should be visible in each of the eight groups in sections (b) and (d) under image acquisition at 6 MV.

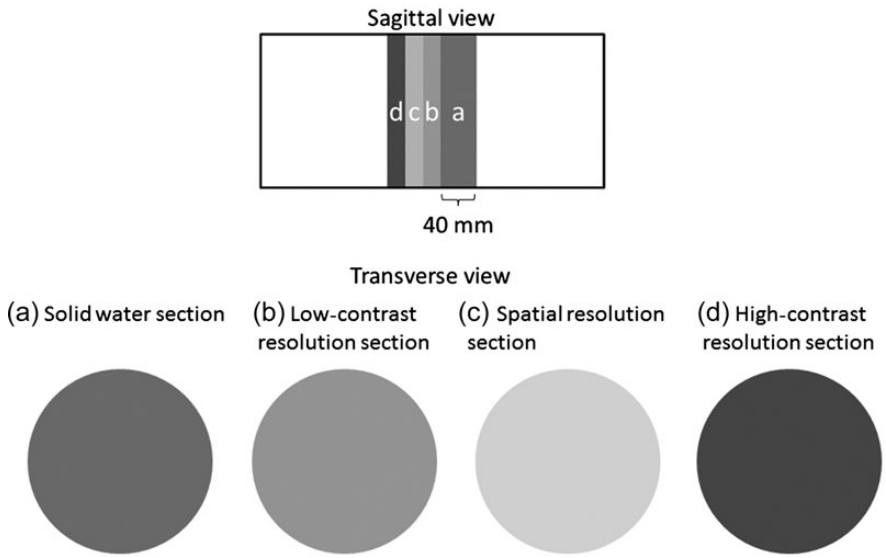

Fig. 2. Four solid sections of the EMMA phantom in sagittal and transverse view. These sections in transverse view consist of (**a**) solid water section, (**b**) low-contrast resolution section, (**c**) spatial resolution section, and (**d**) high-contrast resolution section, respectively.

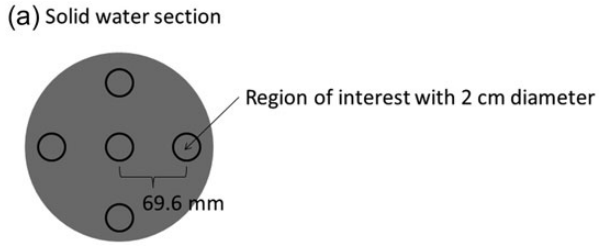

Fig. 3. Five ROIs in the solid water section. Four peripheral ROIs are placed, evenly separated by 69.6 mm from the center of the phantom. The diameter of each ROI is 2 cm.

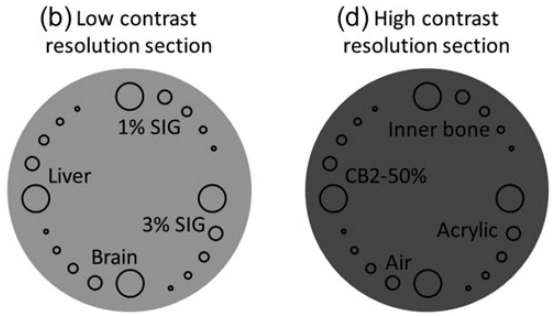

Fig. 4. Low-contrast resolution section (**b**), and high-contrast section (**d**) of the EMMA phantom. Each section has inserts of four different materials, namely (b) brain, liver, 1% SIG, and 3% SIG, and (d) air, CB2-50%, inner bone, and acrylic. The diameter of the five rods for each material is 2, 1, 0.7, 0.5 and 0.3 cm, respectively. SIG means standard imaging grade, which is the background material. CB2-50% means $CaCO_3$.

Different material rods in section (d) were also used to calculate the contrast-to-noise ratios (*CNR*) as presented by Gayou *et al.* [14]. The equation for *CNR* was:

$$CNR = \frac{|S - S_{BG}|}{\sigma}, \quad (1)$$

where S and S_{BG} are the mean pixel values in an insert and the background region surrounding the insert, respectively, and σ is the average standard deviation of the pixel value in the insert and the background. Since this analysis was a quantitative evaluation and the position of each rod and of the background region was clearly defined, each ROI of 2-cm diameter was automatically set to its position in the same manner as in pixel uniformity analysis, as shown in Fig. 3. With regard to the background region after the image was rotated counterclockwise 20°, the ROI at the same position was used for calculation.

Section (c) was used to analyze the spatial resolution of the image. This section contained 11 bar groups, each group of which contained 5 bars, arranged so that each group had a different resolution, as shown in Fig. 5.

Table 1. Physical density and relative electron density of materials with respect to background

Section	Material	Physical density (g/cm^3)	Electron density
ii	Brain	1.05	1.04
ii	Liver	1.09	1.06
ii	1% SIG	1.03	1.00
ii	3% SIG	1.05	1.02
iv	Air	0.00	0.00
iv	CB2-50%	1.56	1.47
iv	Inner bone	1.14	1.08
iv	Acrylic	1.18	1.16

SIG = standard imaging grade of background material, CB2-50%, $CaCO_3$.

Table 2. Number of rods that should be visible in each of the eight groups in 6-MV image acquisition

Section	Material	Visible rods count
ii	Brain	1
ii	Liver	2
ii	1% SIG	0
ii	3% SIG	0
iv	Air	5
iv	CB2-50%	5
iv	Inner bone	4
iv	Acrylic	4

SIG = standard imaging grade of background material, CB2-50%, $CaCO_3$.

Table 3 shows the specification of the chart for each bar group. This is a qualitative analysis based on the number of bars that are visible on the image in which we determine how many groups (each with five line pairs) are visible. The expected results for this test using 6-MV image acquisitions are that the largest to the sixth-largest line group (corresponding to 0.30 LP/mm); in other words, the Nyquist frequency was calculated as 1 divided by twice the sampling frequency of 1.67 mm should be visible with all five dark lines distinctly visible, whereas lines 7–11 should not be resolvable, in accordance with the limitations of current imaging technology.

RESULTS

Figure 6 shows positional errors of the measured positions of the 12 beads with respect to the expected positions from 100 measurements. All beads were within the recommended ±2 mm position precision in all three directions. For the *x*-axis,

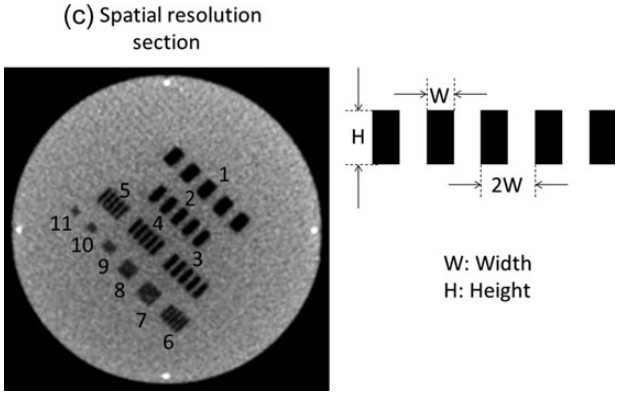

Fig. 5. Spatial resolution section (**c**) of the EMMA phantom containing 11 bar groups with different numbers of line pairs per millimeter. Width of each line pair is labeled 'W' and the height is labeled 'H'.

Table 3. Specification of the chart for each bar group and Nyquist frequency in line pairs per millimeter calculated by width

Bar group	W (mm)	H (mm)	LP/mm
1	7.5	12.0	0.067
2	5.0	12.0	0.1
3	3.3	12.0	0.15
4	2.5	12.0	0.2
5	2.0	12.0	0.25
6	1.67	12.0	0.3
7	1.25	12.0	0.4
8	1.0	10.0	0.5
9	0.83	6.6	0.6
10	0.62	5.0	0.8
11	0.5	4.5	1.0

W = width, H = height.

positional errors at 12 o'clock in all planes (head 10 cm, center, and foot 10 cm) were positive values, while those at 6 o'clock in all planes were negative. For the *y*-axis, positional errors at 3 o'clock in all planes were positive values, while those at 9 o'clock in all planes were negative. This pattern suggests that placement of the EMMA phantom might have been biased slightly toward the clockwise direction in each manual setup. For the *z*- axis, positional errors in the two center and head 10-cm planes were negative values, while those in the foot 10-cm plane were positive. However, uncertainties in the subjective, user-dependent placement of the reference point at the center of the bead might have contributed to these variations.

Figure 7 shows the mean pixel value and one standard deviation for the ROI at the center position, and the difference pixel value at each ROI of 3, 6, 9 and 12 o'clock compared with the center position from 100 measurements. The measured values of two of the 100 measurements for mean pixel value were outside the range of – 30 to +42 (shown in black arrows), at – 40 and +203. All values were within tolerance after the adjustment in beam output for cone-beam CT acquisition. Other values at the second black arrow for SD, 3, 6, 9 and 12 o'clock were also outside the tolerance range. After the adjustment of beam output for cone-beam CT acquisition, these values were within the tolerance range. Apart from these two occurrences, other pixel values for the mean and SD at each ROI position were within the tolerance range.

Figure 8 shows the visible rod counts at the low- and high-contrast resolution sections for various materials from 100 measurements. For the low-contrast resolution section, all materials at up to the diameter specified by the vendor were visible. For the liver rod material, 95 of 100 measurements were more visible than expected, as were 83 of 100 measurements for the brain. For the high-contrast resolution section, all materials with up to the specified diameter by the vendor were also visible.

Figure 9 shows the *CNR* for the three different material rods of CB2-50%, inner bone, and acrylic from 100 measurements. The *CNR* value of CB2-50% was 15.9 ± 0.8 (mean ± SD), which was remarkably higher than those of inner bone (2.5 ± 0.2) and acrylic (3.7 ± 0.2) considering the electron density of each material.

For the evaluation of spatial resolution section by visual inspection, bars in Group 6, that is up to 0.3 LP/mm, were clearly visible for 100 measurements.

DISCUSSION

Imaging performance of MV-CBCT was evaluated with regard to geometrical distortion and image quality for ~ 1 year using 100 measurements. Although the vendor has recommended that the QA used for this study should be performed every month, we changed this frequency to a weekly basis in order to identify subtle changes in characteristics, such as in geometrical distortion and imaging quality, and to evaluate whether the 1-month frequency was valid. In this regard, the AAPM TG-147 report also states that the frequency of the test may be increased upon vendor recommendation [15]. For geometrical distortion, relative position errors of all beads were within the 2-mm tolerance specified by the vendor. Figure 10 shows a vector diagram of positional errors in the central plane in axial view. We performed the QA test 100 times over a period of ~ 1 year, but the tendency identified in Fig. 10 was maintained throughout the test period. The values in Fig. 10 represent the mean translational errors in millimeters for 100 measurements. Although the error value was small, with a measurement uncertainty of

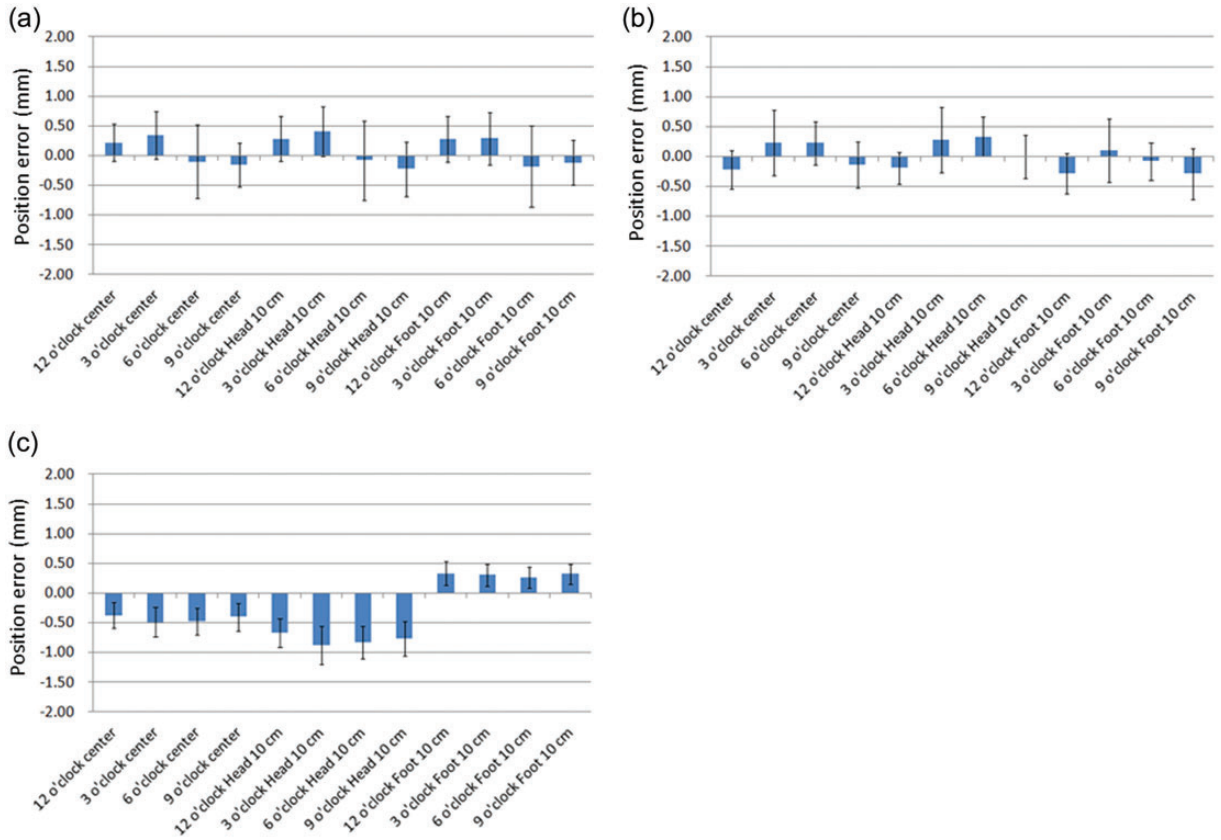

Fig. 6. Positional errors of measured positions of the 12 beads with respect to the expected positions from 100 measurements in the *x*, *y* and *z* axes. The vertical axes show the positional errors of relative lateral (**a**: *x*-axis), vertical (**b**: *y*-axis), and longitudinal (**c**: *z*-axis) measured positions of the 12 beads embedded in the EMMA phantom, with respect to their nominal values at their own bead positions. Each bar presents the mean value from 100 measurements, and the error bar means one standard deviation.

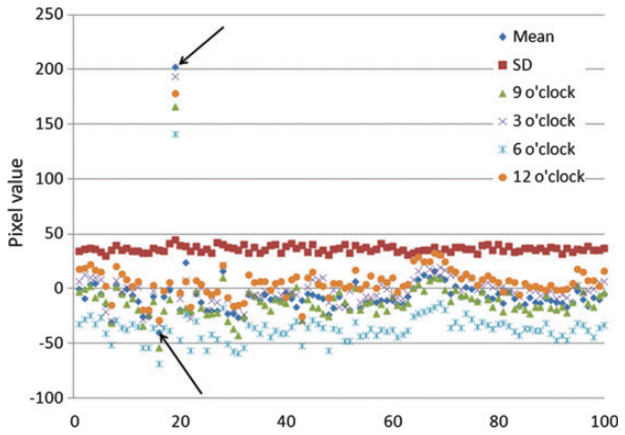

Fig. 7. Mean pixel value and 1 SD for the ROI at the center position, and difference in pixel value at each ROI of 3, 6, 9 and 12 o'clock compared with the center position from 100 measurements. The vertical axis shows the pixel value of the mean and 1 SD of the center ROI and that of the ROI at 3, 6, 9 and 12 o'clock from 100 measurements. SD means one standard deviation. The two black arrows indicate measurements in which the pixel values were out of tolerance.

0.14 mm (calculated from the minimum resolution of 0.27 mm divided by 2), vector sums at the four positions of 3, 6, 9 and 12 o'clock might indicate a tendency to rotational error of $0.11 \pm 0.22°$ (mean ± SD) from the 100 measurements with respect to the *z*-axis in the clockwise direction. Figure 11 shows axial and coronal views of a bucket filled with water taken by MV-CBCT. We confirmed that the water plane was slightly tilted by 0.27° in the clockwise direction on the axial image, and that the image was asymmetric in the left-to-right direction in the coronal image. The water plane should clearly be parallel to a floor, according to gravity. We interpret this strange phenomenon to mean that the geometry calibration for MV-CBCT acquisition is not perfect. Pouliot *et al.* described the geometry calibration procedure in detail [5]. After the geometry phantom was carefully aligned around the machine isocenter, an image was acquired for each of the 200 gantry angles of the cone beam arc. The lookup tables, which are 4×4 matrices, consist of the rotation and translation for each projection image, and are automatically created to correct errors in the vertical and horizontal scale and skew of the detector that can be caused

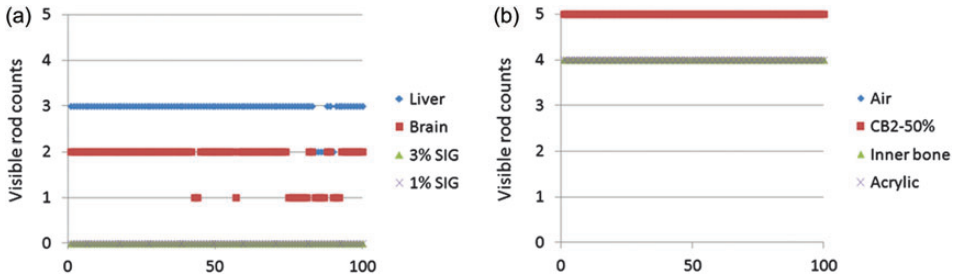

Fig. 8. Visible rod counts at low- and high-contrast resolution sections for various materials from 100 measurements. The vertical axis shows the visible rod counts for each material at the (**a**) low-contrast resolution section, and (**b**) high-contrast resolution section from 100 measurements. For both contrast sections the visible rod counts were within the tolerance specified by the vendor.

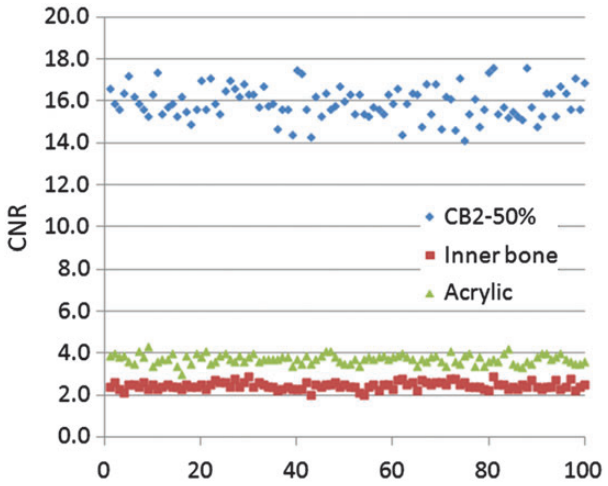

Fig. 9. Contrast-to-noise ratio (*CNR*) for CB2-50%, inner bone and acrylic from 100 measurements.

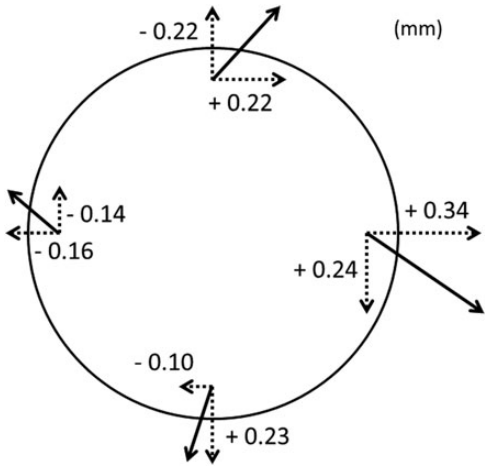

Fig. 10. Vector diagram of the positional errors in the central plane in axial view. Dashed arrows show the mean translational errors in millimeters for 100 measurements. Solid arrows show the vector sum. The size of each vector represents the translational error.

by detector sagging or mispositioning. When the geometry phantom is misaligned with a translational error of a few millimeters or a rotational error of a few degrees, the calibration procedure fails. In that case the lookup tables will not be updated because the offset values for the calibration are large and are regarded by the system as out of the tolerance range. The system does not allow users to determine the tolerance value for the geometric calibration, which means it is a 'black box'. If the size of the error caused by misalignment is small, however, the calibration procedure is performed correctly. In the present study, we found that positional errors in geometrical distortion resulted in geometry calibration with slight misalignment errors, and that these would lead to residual error.

Therefore, according to the results for 100 measurements, the new tolerance values in millimeters for bead positions were established in our department. Table 4 summarized the new tolerance values at the four positions of 3, 6, 9 and 12 o'clock in each axis that were based on the 95% confidence interval (i.e. mean ± 1.96 SD). Those tolerance values were smaller than the vendor specification of 2 mm, and the maximum value for the results was 1.32 mm. Although it was ideal that the tolerance values at any bead's position in each axis were consistent, our tolerance values were considered to be valid, taking into consideration the residual error for the geometry calibration, the manual set-up error of the EMMA phantom, and the manual identification of the bead's position. In terms of the frequency of QA for geometric distortion, the stable results for this study indicate that this can be reasonably performed on a monthly basis.

Image qualities for uniformity, low-contrast resolution, high-contrast resolution, spatial resolution and *CNR* were evaluated. For image uniformity, there were two incidents in 100 measurements in which pixel values of the ROI were out of tolerance, both of which were solved by the adjustment of beam output for cone-beam CT acquisition. Dose output calibration for cone-beam CT when used for image acquisition is performed in our department once a month, which is basically the same period as that used for calibration of the

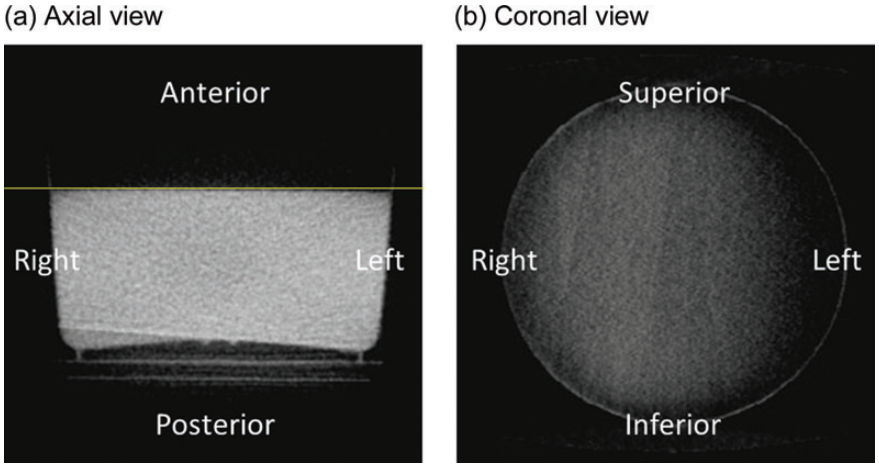

Fig. 11. Image of a water-filled bucket by MV-CBCT acquisition in (**a**) axial and (**b**) coronal views. The coronal image was at the position of the water surface shown by the yellow line in the axial image.

Table 4. The new tolerance values in each axis for bead position based on the results of 100 measurements

Axis	Bead position			
	12 o'clock (mm)	**3 o'clock (mm)**	**6 o'clock (mm)**	**9 o'clock (mm)**
x	−0.39–0.83	−0.45–1.13	−1.32–1.12	−0.89–0.58
y	−0.83–0.40	−0.83–1.31	−0.48–0.94	−0.90–0.63
z	−0.81–0.06	−0.98–0.00	−0.93– − 0.02	−0.87–0.06

treatment beam for X-ray beams and electron beams. Given the difficulty of predicting when such incidents might occur within the 1-month period between calibrations, it is important to check beam output for cone-beam CT as well as the treatment beam on a daily basis, or at least more frequently than on a monthly basis. In terms of the pixel uniformity at each ROI position, the new tolerance values were also established from the results of 100 measurements. Table 5 summarized the new tolerance values at each ROI position of the center, 3, 6, 9 and 12 o'clock that were based on the 95% confidence interval (i.e. mean ± 1.96 SD) and the vendor specification for comparison. Our tolerance values for the mean pixel value and the standard deviation at the center ROI were slightly wider than those of the vendor specification. In contrast, our tolerance values at the four positions of 3, 6, 9 and 12 o'clock were narrower than those of the vendor specification. Therefore, strictly based on the tolerance value, it was considered valid that the vendor specification would be applicable for the center ROI, and that our tolerance values would be applicable for the other ROI positions.

With regard to low-contrast, high-contrast, and spatial resolution, these are based on qualitative evaluation. All visual checks in this study were done by a single person, obviating the question of interobserver error. Manipulation of window width and window level for CBCT images invariably introduces a degree of subjectivity into visual inspection. However, a significant loss in contrast resolution will be detectable. For the purpose of quality control at least, QA should be performed using a consistent image acquisition protocol. However, the MU used for MV-CBCT acquisition in clinical settings depends on treatment site, and efforts to reduce dosage mean that it will usually be < 15 MU. In general, however, the lower the MU, the worse the image quality, and an appropriate setting for image guidance should therefore be sought. With regard to *CNR*, there were no deviations in *CNR* values, as shown in Fig. 9, although two of all the mean pixel values were outside the tolerance, as shown in Fig. 7. Even though the mean pixel values were outside the tolerance due to the out of calibrated beam output of MV-CBCT, the difference between the mean value of the CB2-50% rod and the background region was close to that for the normal beam output of MV-CBCT, and the standard deviation of the difference between the CB2-50% rod and the background region was also close to that for the normal beam output of MV-CBCT. Therefore the *CNR* value was not affected. Gayou *et al.* presented *CNR* values of ~ 8.8, 3.0 and 4.2 for CB2-50%, inner bone and acrylic, respectively [14], using the same machine specifications as in our present study. These past results and our present results were similar for inner bone and acrylic, but our *CNR* findings for CB2-50% were higher as a result of the improvement of signal-to-noise ratio for the use of 5-mm multiple plane reconstruction. In the case of the use of a 1-mm reconstruction, our *CNR* results for CB2-50% were 9.7 ± 0.8 (mean ± SD), which are close to those of Gayou *et al.*'s study. They reported that when field width in the longitudinal direction decreases from 27.4 to 5 cm, *CNR* increases by about 20%.

Table 5. The new tolerance values and the vendor specification for the pixel uniformity at each ROI position based on the results of 100 measurements

		Pixel value (a.u.)	
ROI position	**Evaluation item**	**Our tolerance value**	**Vendor specification**
Center	Mean	−52–40	−30–42
Center	SD	31–42	26–42
12 o'clock	Mean difference from the center	−34–48	−80–80
3 o'clock	Mean difference from the center	−44–44	−80–80
6 o'clock	Mean difference from the center	−76–4	−80–80
9 o'clock	Mean difference from the center	−52–30	−80–80

SD = standard deviation, a.u. = arbitrary unit.

Given the balance between imaging dose and image quality, we consider that decreasing field size in the longitudinal direction is a convenient method for increasing *CNR* and reducing imaging dose. Although there are no vendor specifications for the *CNR*, we have established the tolerance values of 14.4–17.5, 2.1–2.8 and 3.3–4.2 for CB2-50%, inner bone and acrylic, respectively. These tolerance values were based on the 95% confidence interval (i.e. mean ± 1.96 SD), using our results for the 100 measurements.

CONCLUSION

Here, we evaluated the long-term stability of an MV-CBCT device during the evaluation period, and confirmed the suitability of the vendor's QA process. Based on our results, the new tolerance levels for bead position, pixel uniformity and the *CNR* were established. Those tolerance levels will be useful data as the reference of periodical quality control in our department. Our findings highlight the importance of recognizing the presence of a residual error in geometric distortion during geometric calibration of the MV-CBCT. To ensure image quality, stability of the beam output should be evaluated more frequently than the vendor's recommended monthly evaluation cycle.

REFERENCES

1. Lattanzi J, McNeely S, Hanlon A *et al*. Daily CT localization for correcting portal errors in the treatment of prostate cancer. *Int J Radiat Oncol Biol Phys* 1998;**41**:1079–86.
2. Mackie TR, Kapatoes J, Ruchala K *et al*. Image guidance for precise conformal radiotherapy. *Int J Radiat Oncol Biol Phys* 2003;**56**:89–105.
3. Jaffray DA, Drake DG, Moreau M *et al*. A radiographic and tomographic imaging system integrated into a medical linear accelerator for localization of bone and soft-tissue targets. *Int J Radiat Oncol Biol Phys* 1999;**45**:773–89.
4. Uematsu M, Fukui T, Shioda A *et al*. A dual computed tomography linear accelerator unit for stereotactic radiation therapy: a new approach without cranially fixated stereotactic frames. *Int J Radiat Oncol Biol Phys* 1996;**5**:587–92.
5. Pouliot J, Bani-Hashemi A, Chen J *et al*. Low-dose megavoltage cone-beam CT for radiation therapy. *Int J Radiat Oncol Biol Phys* 2005;**61**:552–60.
6. Jaffray DA, Siewerdsen JH. Cone-beam computed tomography with a flat-panel imager: initial performance characterization. *Med Phys* 2000;**27**:1311–23.
7. Herman MG. Clinical use of electronic portal imaging. *Semin Radiat Oncol* 2005;**15**:157–67.
8. Johnston H, Hilts M, Beckham W *et al*. 3D ultrasound for prostate localization in radiation therapy: a comparison with implanted fiducial markers. *Med Phys* 2008;**35**:2403–13.
9. Verellen D, Soete G, Linthout N *et al*. Quality assurance of a system for improved target localization and patient set-up that combines real-time infrared tracking and stereotactic X-ray imaging. *Radiother Oncol* 2003;**67**:129–41.
10. Klein EE, Hanley J, Bayouth J *et al*. Task group 142 report: quality assurance of medical accelerators. *Med Phys* 2009;**36**:4197–212.
11. Siewerdsen JH, Jaffray DA. Optimization of x-ray imaging geometry (with specific application to flat-panel cone-beam computed tomography). *Med Phys* 2000;**27**:1903–14.
12. Akino Y, Koizumi M, Sumida I *et al*. Megavoltage cone beam computed tomography dose and the necessity of reoptimization for imaging dose-integrated intensity-modulated radiotherapy for prostate cancer. *Int J Radiat Oncol Biol Phys* 2012;**82**:1715–22.
13. Abou-Elenein HS, Attalla EM, Ammar H *et al*. Megavoltage cone beam computed tomography: Commissioning and evaluation of patient dose. *J Med Phys* 2011;**36**:205–12.
14. Gayou O, Miften M. Commissioning and clinical implementation of a mega-voltage cone beam CT system for treatment localization. *Med Phys* 2007;**34**:3183–92.
15. Willoughby T, Lehmann J, Bencomo JA *et al*. Quality assurance for nonradiographic radiotherapy localization and positioning systems: Report of Task Group 147. *Med Phys* 2012;**39**:1728–47.